nature communications

Article

https://doi.org/10.1038/s41467-025-66053-8

Multi-stage power-to-water battery synergizes flexible energy storage and efficient atmospheric water harvesting

Received: 15 April 2025

Accepted: 27 October 2025

Published online: 12 December 2025

Check for updates

Haosheng Lin[1,2,7], Yan Song[3,4,7], Zhixiong Ding[1], Yunren Sui[1], Zengguang Sui[1], Fuxiang Li[1], Jia Zhu[3,4,5,6] ✉ & Wei Wu[1,2] ✉

We propose and demonstrate a multi-stage power-to-water (MSP2W) battery that synergizes flexible energy storage and atmospheric water harvesting (AWH) to address renewable energy intermittency and freshwater scarcity simultaneously. This system integrates high-temperature magnesium oxide-based thermal energy storage (TES) with a modular multi-stage AWH device, using a Reline-based ternary solution to enhance sorption kinetics and enable efficient scalability. The multi-stage AWH configuration, with up to three stages, enhances water production by 51%, reducing energy consumption by 26%, consistent with theoretical analysis. The MSP2W prototype achieves daily water production of 3060 g, fully meeting an adult's demand. The specific energy consumption is as low as 1.13 kWh kg^{-1}, outperforming existing active AWH systems. The niche area of MSP2W is identified, even competing with desalination costs (<20 USD ton^{-1} of optimal levelized cost of water). The system demonstrates scalability and cost-effectiveness, with the potential to fully mitigate water scarcity in regions with high renewable energy surpluses.

Energy storage systems (ESSs) have gained significant global attention due to their potential to align renewable energy supply (e.g., solar and wind power) with consumer demand, a major barrier to the widespread adoption of renewable energy[1,2]. Nonetheless, contemporary ESSs face challenges like terrain-specific demands, inefficiency, and profitability concerns[3–9]. Consequently, there is an increasing need to develop ESSs that are scalable, sustainable, and cost-effective for versatile renewable energy use[10].

While much of the focus has been on improving the performance of ESS, an important but overlooked application is the integration of ESS with atmospheric water harvesting (AWH) systems, which could significantly address water scarcity. Many areas rich in renewable energy resources, such as solar and wind, are often plagued by water scarcity[11]. These regions, typically characterized by high solar radiation and/or strong winds, lack sufficient water resources to support local populations. This presents a unique opportunity to use surplus renewable energy for on-site water production. To quantify this potential, we introduce the water-energy synergy index (WESI), which combines local water stress and renewable energy surplus. The WESI is calculated by multiplying the normalized water stress index with the normalized energy redundancy index, which measures the regional surplus renewable energy. A higher WESI value indicates greater potential for using renewable energy to alleviate water scarcity. As shown in Fig. 1a, inland areas like northwestern China and the Middle East, where abundant renewable energy coincides with high water stress, are suitable for utilizing surplus energy to support water production.

Sorption-based AWH is an emerging and promising inland water production technology[12–14], but the water yield from these systems

[1]School of Energy and Environment, City University of Hong Kong, Hong Kong, China. [2]City University of Hong Kong Shenzhen Research Institute, Shenzhen, China. [3]School of Sustainable Energy and Resources, Nanjing University, Suzhou, China. [4]Frontiers Science Center for Critical Earth Material Cycling, Nanjing University, Nanjing, China. [5]National Laboratory of Solid State Microstructures, Nanjing University, Nanjing, China. [6]College of Engineering and Applied Sciences, Nanjing University, Nanjing, China. [7]These authors contributed equally: Haosheng Lin, Yan Song. ✉e-mail: jiazhu@nju.edu.cn; weiwu53@cityu.edu.hk

https://doi.org/10.1038/s41467-025-66053-8

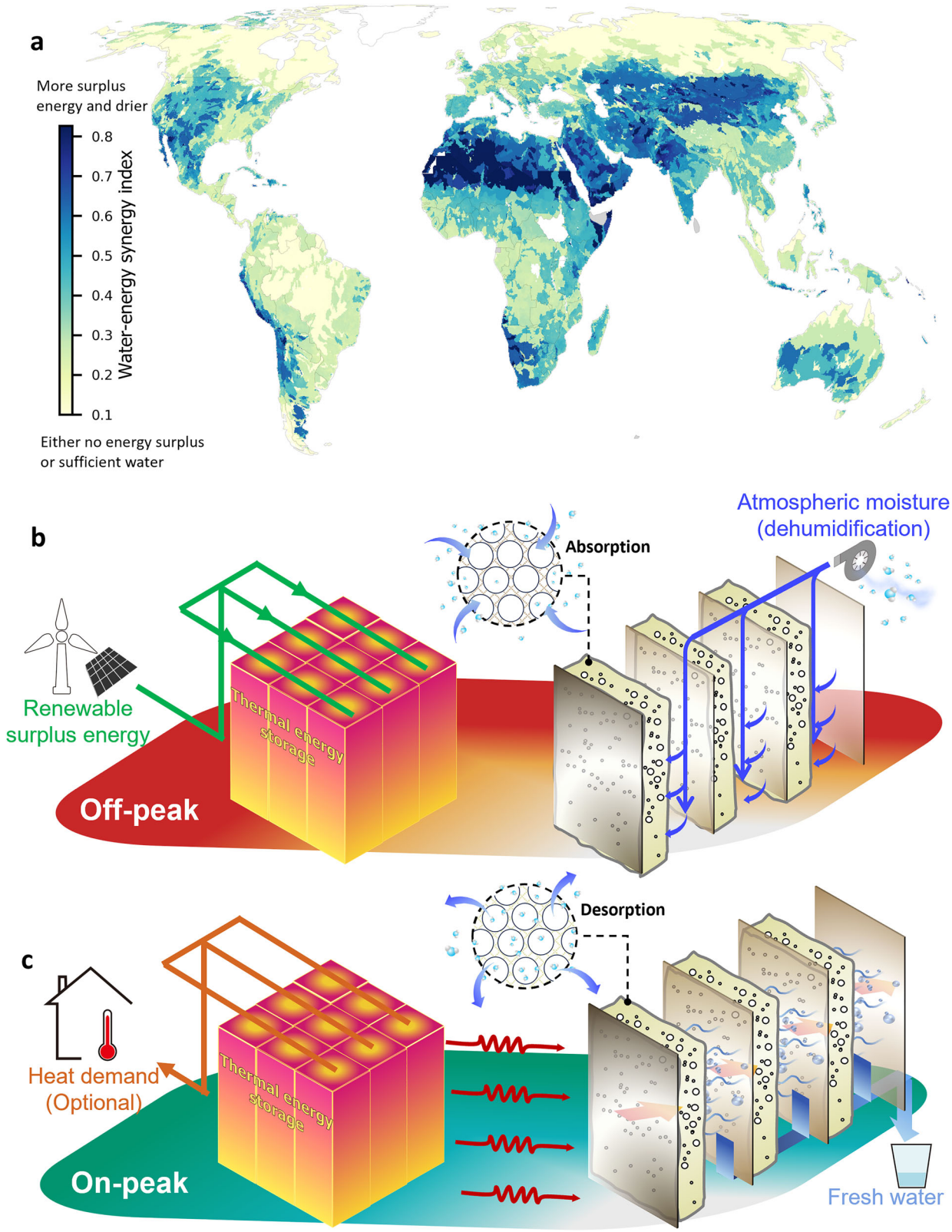

Fig. 1 | Water-energy synergy opportunities in renewable energy-rich but water-scarce regions, and the corresponding solution by adopting MSP2W. **a** Water-energy synergy index (WESI) at a global view. The larger the value, the greater the surplus of new energy and the drier the conditions in the area; conversely, the smaller the value, the lower the surplus of new energy (or the more abundant the water resources). Refer to Supplementary Method 1 for detailed calculations. **b** MSP2W is proposed to cost-effectively store the surplus renewable energy for sorption-based AWH. During off-peak hours, renewable energy is stored as high-temperature thermal energy. Meanwhile, the MSAWH absorbs moisture in batches from the ambient environment. **c** During on-peak hours, the stored thermal energy is used for desorption of the multi-stage water harvester.

remains low[15], because several obstacles hinder the practical use. The first challenge is the limited water uptake or slow sorption kinetics of most materials (Supplementary Fig. 1). Liquid sorbents, such as hygroscopic salts, exhibit high capacity but slow sorption kinetics[16–18], while solid sorbents like metal-organic frameworks (MOFs) and zeolites show faster kinetics but lower water uptake[19–24]. The second challenge is the unscalability and unpredictability of passive solar-based AWH systems. Variations in solar energy result in fluctuating water production. The low energy density of solar energy necessitates large-scale sorption beds, which impairs system efficiency. For example, the AWH system uses MOFs or porous-matrix composite sorbents, while the small-scale tests demonstrate fast water uptake, scaling up the system to pursue higher water production results in a significant drop in sorption efficiency[25,26].

Lastly, active AWH systems, while capable of providing higher water production, face energy-intensive production, with estimates of 2–10 MWh of electricity required to produce one ton of water. This results in significant pressure on the grid when scaled up[25–31]. This high consumption arises from heating the sorbent to high temperatures for desorption, while the condensation heat, near the temperature of the sorbent, dissipates into the surroundings, resulting in significant energy loss. Some methods have the potential to address this issue. For example, the concept of multi-stage, previously applied in solar seawater distillation, has demonstrated substantial increases in desalination efficiency[32,33]. However, few studies focus on multi-stage AWH (MSAWH) technologies. The only study has revealed a 17% improvement in solar zeolite-based dual-stage AWH systems over single-stage systems[22]. Meanwhile, substantial theoretical insights into MSAWH are still lacking.

Here, we propose a multi-stage power-to-water (MSP2W) battery, an approach across concepts, theory, materials, and devices, designed to address energy-water nexus challenges effectively. The MSP2W battery is composed of a thermal energy storage (TES) unit and an MSAWH unit. Here, "battery" means any system that cyclically stores and releases energy, akin to thermal or carbon batteries[34,35]. The main advantage of TES over direct solar energy is to manage energy variability and intermittency. Renewable energy generation fluctuates due to weather and time of day, making real-time supply-demand mismatching. TES stores surplus energy during excess generation periods for later use, ensuring efficient operation. Proven practical and cost-effective in prior research[16], the P2W battery can economically store surplus renewable energy for efficient AWH, reducing grid strain. Besides, the MSAWH unit involves Reline-based ternary solution (RTS-X) with high capacity and resistance to crystallization. Implemented in an active sandwich-structure liquid absorption bed (SLAB), the RTS ensures both high capacity, fast kinetics, and excellent stability.

As shown in Fig. 1b, during off-peak hours (excess electricity is available), MSP2W stores renewable energy as low-cost, high-density, and high-temperature thermal energy, making full use of resources. Meanwhile, the MSAWH absorbs moisture in batches from the atmosphere, ensuring fast sorption kinetics and expanding absorption capacity. During peak hours (Fig. 1c), the stored thermal energy is discharged to elevate the temperature of the sorbent in the first stage, leading to the desorption of water vapor. The water vapor condenses in the first-stage condenser, releasing latent heat. The latent heat is then transferred to the subsequent stages until the final stage, so that the energy efficiency is improved by utilizing cascading thermal energy.

The key strengths of the MSP2W system are its flexibility and cost-effectiveness. The TES unit allows the energy storage process and water vapor capture process to operate independently. The energy storage process is inexpensive and thus has a huge charging capacity, allowing it to fully use the low- or negative-prices electricity, without waiting for the vapor capture to happen. Similarly, the water vapor release process (desorption) does not depend on whether there is low- or negative-prices electricity. As long as the TES has reached a certain temperature, the system can start desorption, even if the TES is still in the process of storing energy. Additionally, the system can even store energy and desorption simultaneously. Moreover, the desorption process is fast (1–2 h), due to the high temperature of TES. Based on this concept, MSP2W can harness local surplus renewable energy, support flexible power grids, and provide essential water supplies simultaneously.

Results

Theoretical limit of MSP2W

The thermodynamic model is foundational to optimizing MSAWH (Fig. 2a), providing critical insights that inform both material selection and device configuration.

Our theoretical steady-state model shows that the multi-stage configuration can enhance AWH production limit (Fig. 2b, c), but increasing the number of stages does not always lead to higher water production (Supplementary Fig. 10). The model demonstrates a nonlinear and non-positive correlation between the number of stages and water production, particularly under moderate humidity. This contrasts with conventional wisdom from multi-stage solar desalination, which often employs more than 10 stages to maximize efficiency. This can be explained from the P-T-U perspective (Supplementary Note 1), that the materials with high sorption capacity (such as LiCl) will have more advantages (Fig. 2d, e). To validate these findings, we introduce a dynamic model that incorporates transient effects like heating, heat transfer, mass transfer within the sorbent, phase changes, and wall heat loss. Dynamic model confirms that a 3-stage configuration maximizes water production under moderate humidity (10–15 g kg^{-1}), while additional stages beyond this threshold result in diminishing returns due to diminishing temperature gradients and increasing heat losses (Fig. 2f). Supplementary Fig. 14 illustrates the temperature variations and water harvesting performance across stages in different configurations, explaining this discrepancy. Water harvesting sharply declines from the 3-stage onward, due to insufficient desorption resulting from temperature-difference drops in intermediate and subsequent stages, leading to water not being released from the sorbent, and the increased heat dissipation from the sidewalls or solar absorber, evident in Figs. S15–S17. This insight directly informed our experimental decisions, preventing unnecessary complexity in the prototype and avoiding over-engineering, which would have otherwise reduced the system's performance.

We further analyze important parameters of MSAWH, including heating power, air gap thickness, sorbents, and sorbent thickness. Decreasing heating power significantly reduces performance, as a 40% cut in heating power leads to a 70% drop in production (Supplementary Fig. 20a), demonstrating the adverse effects of unstable solar radiation and necessitating the high-temperature TES. Additionally, increasing the air gap from 2 to 20 mm decreases water harvest by 12% (Supplementary Fig. 20b), irrespective of sorbent equilibrium, due to increased mass transfer resistance. As shown in the Lewis relationship (Eq. S26), the mass transfer resistance in the air gap is directly proportional to thermal resistance. Notably, heat loss from the front solar absorber at almost 600 W m^{-2}, vastly exceeds that of its counterparts, around 70 W m^{-2}. Since sorbent thickness increases the amount of sorbent, it is positively correlated with water production (Supplementary Fig. 20c). A dynamic result (Supplementary Note 3) of different sorbents supports steady-state simulation results and demonstrates slower kinetics in LiCl. Therefore, although liquid sorbents exhibit superior water harvesting performance, enhancing both the heating power and the sorption kinetics is essential to fully exploit their potential within MSAWH. Theoretical predictions guide the experimental design, ensuring that each stage contributes effectively to the system's overall performance (Supplementary Fig. 22).

https://doi.org/10.1038/s41467-025-66053-8

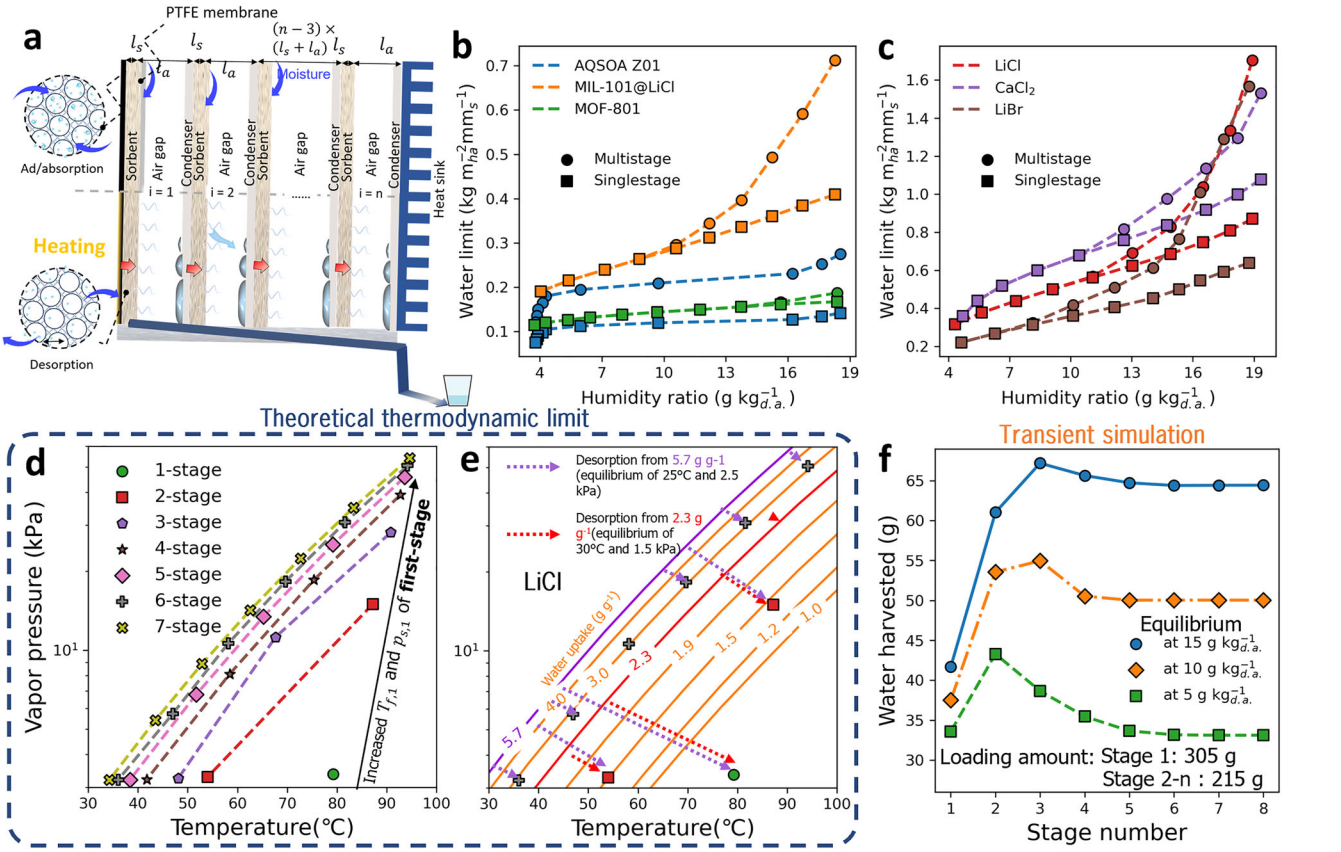

Fig. 2 | The theoretical limit of MSAWH. The detailed steady-state model is available in Supplementary Method 2. The detailed dynamic model is presented in Supplementary Method 3, with validation provided in Supplementary Note 2. **a** Concept of MSAWH. **b** Daily AWH limit of typical solid sorbents at the optimal stage number and 25 °C (temperature and humidity ratio of ambient air). The harvested water quantity will be expressed in kg per heating area per millimeter of sorbent thickness (kg m_{ha}^{-2} mm_s^{-1}). Sorbent quantity is represented by thickness due to the varying densities of different sorbents. **c** Daily AWH limit of typical liquid sorbents at the optimal stage number and 25 °C. The quantity of water is also represented as kg m_{ha}^{-2} mm_s^{-1}. **d** Pressure–temperature (P–T) distribution across sorbent layers for varying stage numbers. Given that the thermal resistance of the sorbents is overlooked, both temperature and water vapor distributions of distinct sorbents are the same. Detailed analysis can be referred to Supplementary Note 3. **e** LiCl water uptake variations during the desorption for 1-stage, 2-stage, and 6-stage configurations. The arrows represent the change in the equilibrium state of water uptake of LiCl during desorption. **f** Water production of AQSOA Z01-based MSAWH across various stage numbers at three different equilibrium humidity ratios and a temperature of 25 °C.

Fabrication and characterization of RTS and SLAB

The Reline-based ternary solution (RTS-X, where X indicates the percentage of Reline in RTS; for example, RTS-20 contains 20 wt% of Reline) is selected for use in the MSP2W system due to its high sorption capacity, crystallization-free, and superior recyclability compared to conventional sorbents. Deep eutectic solvents (DESs) are widely recognized as ionic liquids, sharing many characteristics with ionic liquids, such as consisting of large, nonsymmetric ions with low lattice energy[36]. They are typically produced through the complexation of a quaternary ammonium salt with a metal salt or a hydrogen bond donor[36]. For instance, in Reline, the charge delocalization via hydrogen bonding between a halide ion in choline chloride (ChCl) and the hydrogen bond donor (Urea) reduces the crystallization point compared to that of the individual components. However, there is still room for improvement in DES water uptake capacity. To address this, we incorporated hygroscopic salt into the DES to further improve the water sorption performance, resulting in the RTS-X, as depicted in Fig. 3a. RTS effectively prevents crystallization, thereby avoiding sorbent circulation blockage and circumventing kinetic impedance. Therefore, RTS can have its kinetics significantly improved through measures such as spraying or cooling, which accelerate diffusion and reduce sorbent vapor pressure.

RTS-X significantly mitigates crystallization compared to LiCl (Fig. 3b). At 40 °C, LiCl crystallizes at a mass fraction of 48%, whereas RTS-20 and RTS-30 crystallize at 56% and 59%, respectively; at 50 °C, the corresponding values for RTS-20 and RTS-30 are 58% and 63%, respectively. In addition to the decrease in salt content, a hypothesis is proposed that DES delayed crystallization: Fourier-transform infrared (FTIR) analysis of RTS-X (Fig. 3c) shows that its characteristic peaks are primarily Reline, with peaks around 3300 cm^{-1}, 1600 cm^{-1}, and 1450 cm^{-1}, exhibiting a blue shift relative to pure Reline, which can be attributed to hydrogen bonding increases, the O–H bonds in water and interactions between chloride ions and water molecules shorten, raising the vibration frequency[37], reflecting enhanced hydrogen bonding that stabilizes the liquid phase[38]. These hydrogen bonds lower the solution free energy, making it harder for salt ions to form an ordered lattice, thereby significantly reducing or even suppressing crystallization[39]. This stable liquid structure not only lowers the crystallization temperature but also inhibits the nucleation and growth of crystals[40], consistent with the observed behavior of RTS-X. Also noted that hydrogen bonding in RTS has little effect on evaporation enthalpy according to DSC testing in Supplementary Fig. 23, supporting its effectiveness in desorption. It is also noteworthy that RTS remains suspended at the crystallization point, as shown in Figs. S24 and S25. This characteristic also helps prevent blockage during circulation. Additionally, the water sorption isotherms for LiCl, RTS-20, and Reline are presented in Fig. 3d, which demonstrates that Reline not only resists crystallization but also

https://doi.org/10.1038/s41467-025-66053-8

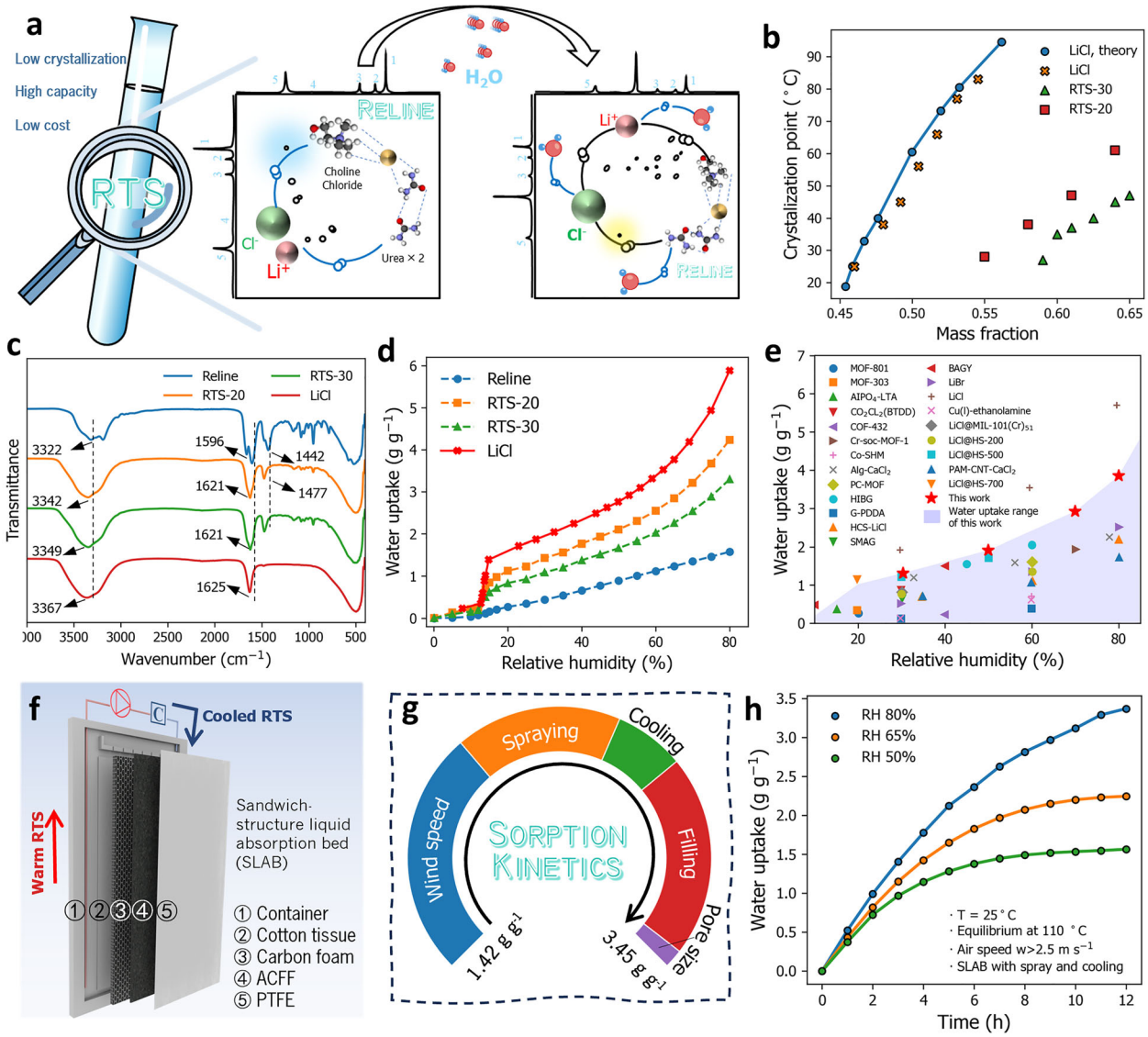

Fig. 3 | Fabrication and characterization of RTS and SLAB. a RTS is composed of both strong sorbents: Reline and LiCl, which have high sorption capacity and low crystallization temperature. **b** Crystallization curves of LiCl solution and RTSs. **c** FTIR spectroscopy curves of LiCl solution, Reline, and RTSs. **d** Vapor adsorption isotherms for RTS and DES, and theoretical isotherms for LiCl. **e** Water uptake comparison between RTS and state-of-the-art sorption materials. The detailed information about reported AWH sorbents is listed in Supplementary Table 5. **f** Schematic of SLAB. **g** Contribution of different factors to the sorption kinetics enhancement of SLAB. **h** Sorption kinetics of SLAB under different relative humidities.

serves as an effective sorbent, with water uptake reaching 0.42 g g^{-1}, 0.93 g g^{-1}, and 1.23 g g^{-1} at 30%, 50%, and 70% RH, respectively. Moreover, forming the ternary solution with LiCl significantly enhances the water uptake of Reline. Compared with RTS-30, RTS-20 has a higher water uptake, reaching 1.56 g g^{-1}, 1.93 g g^{-1}, and 3.02 g g^{-1} at 30%, 50%, and 70% RH, respectively. Remarkably, RTS-20 can absorb more than 420% water by weight under humid conditions (80% RH). Additionally, RTS exhibits a similar S-shaped isotherm to LiCl, with a sudden increase in water uptake to 0.95 g g^{-1} at 17% RH. This indicates that RTS is stable and does not crystallize even at such low humidity levels. Furthermore, RTS demonstrates satisfactory water uptake performance compared to other reported AWH sorbents (Fig. 3e)[21,26,41–54].

The design of the sorption bed is crucial to the efficiency of sorption and desorption processes in real-world water harvesting, yet it is often underexplored. Most studies focus on small-scale sorption dynamics, using milligram-scale samples in controlled environments, such as chambers or TGA, with constant humidity, temperature, and airflow. However, simply scaling up sorbent materials to increase water production is not a straightforward solution, as it can increase the vapor diffusion resistance, impact heat transfer significantly, and thus degrade sorption kinetics[26]. To make up the gap in sorption bed scale, we introduce an active SLAB. Figure 3f illustrates that the SLAB consists of corrosion-resistant, high-temperature-resistant polytetrafluoroethylene (PTFE) and titanium metal, covered by a hydrophobic and breathable PTFE membrane. The top of the SLAB features small holes for pipe access, facilitating solution extraction, cooling, and spraying. From the outer to the inner layer, the SLAB is composed of active carbon fiber felt (ACFF), carbon foam, and cotton tissue. The porous and capillary ACFF expands the specific surface area during absorption, carbon foam serves as a filler to enhance heat and mass exchange during spraying, and the thin cotton tissue increases the heating area during desorption with its capillary action. The necessity of design is demonstrated through scale-down SLAB experiments (Supplementary Fig. 26). Firstly, as shown in Supplementary Fig. 27, we calculate the mass-transfer resistance of SLAB, denoted as R,

https://doi.org/10.1038/s41467-025-66053-8

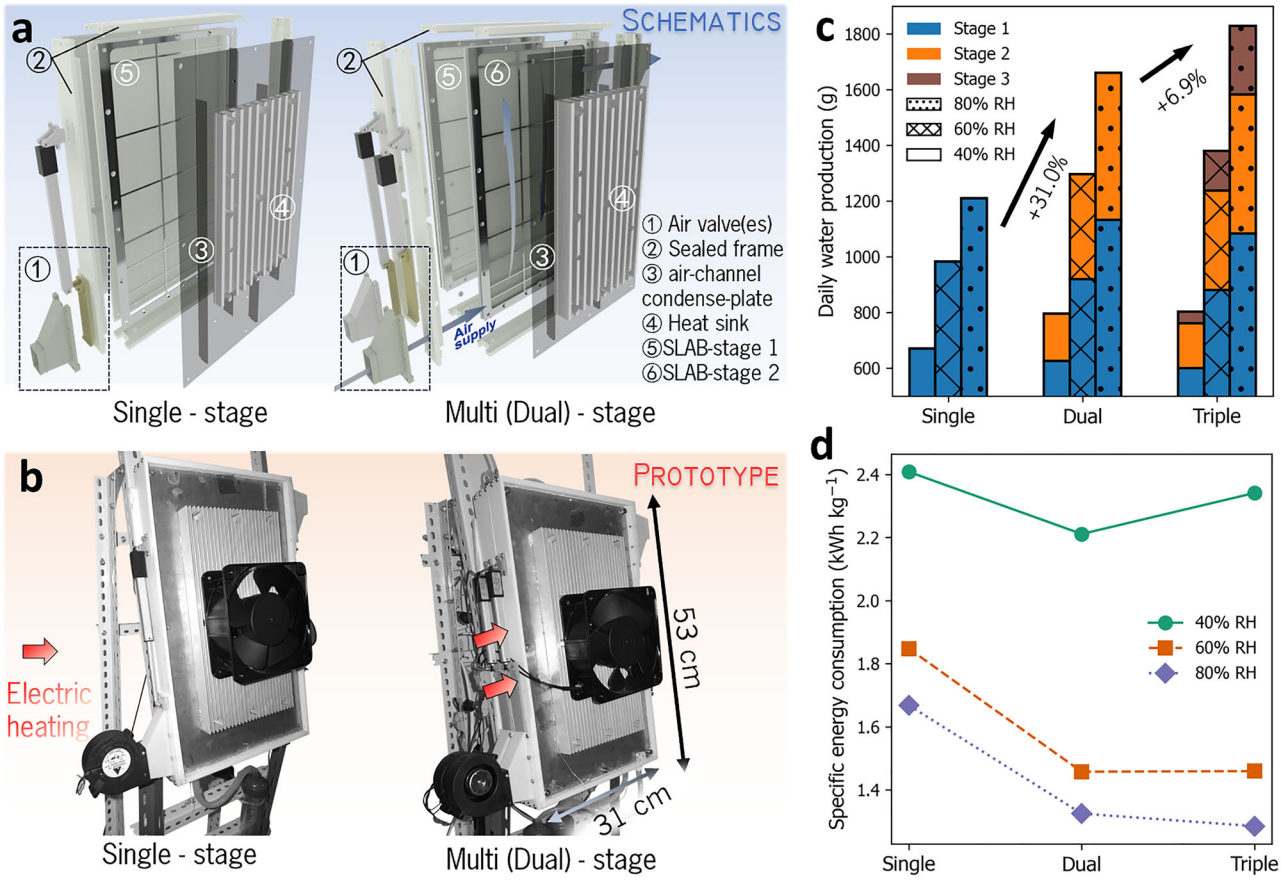

Fig. 4 | Design and optimization of a water harvester. a Schematics of a modular water harvester. **b** Photos of a modular water harvester. **c** Daily water production comparison between various setups and RH conditions. The experiments are shown in Supplementary Movies 1–3. The original experiment results and details can be found in (**a**, **b**) from Supplementary Figs. 37–45. **d** Specific energy consumption comparison between various setups and RH conditions. The original experiment results and details can be found in (**c**) from Supplementary Figs. 37–45.

consisting of:

$$R = R_s(D_s, T) + R_m(l) + R_a(D_a, w) \quad (1)$$

where R_s, R_m, and R_a are the mass-transfer resistance of sorbent, membrane, and air layer, respectively; D_s and D_a are the diffusivities of sorbents and air; T is the temperature of sorbent; l is the pore size of the membrane; w is the speed of airflow.

Based on Eq. 1, we employed several methods to reduce mass transfer resistance. Initial attempts to improve sorbent diffusivity (D_s) through forced circulation had minimal effects (Supplementary Fig. 28a). Increasing airflow from 0.5 m s^{-1} to 3 m s^{-1} significantly raised sorption kinetics from 1.41 g g^{-1} to 2.58 g g^{-1} in 12 h, revealing air layer resistance (R_a) as a main mass-transfer barrier (Supplementary Fig. 29b, c). Multiphysics simulations showed low RH films hindered kinetics, which improved with higher airflow (Supplementary Fig. 29). Further enhancements involved integrating cooling units and optimizing the fillings, which notably increased kinetics to 3.4 g g^{-1} (Supplementary Fig. 28d, e). Initially, the pure-ACFF bed lacked extra fluid supply (Supplementary Fig. 30a), but switching to a sandwich-structure improved fluid delivery for cooling by minimizing capillary water absorption (Supplementary Fig. 30b). The cumulative impact of these methods on kinetics improvement is detailed in Fig. 3g. Compared to the initial setup, the optimized SLAB demonstrated 143% improvement in 12-h kinetics, from 1.42 g g^{-1} to 3.45 g g^{-1}. We also investigated the effect of sorbent-loading amount, demonstrating that increased sorbent-loading enhances total water uptake, but reduces normalized water uptake (Supplementary Fig. 31). The latest SLAB version achieves water uptakes of 3.45 g g^{-1}, 2.46 g g^{-1}, and 1.59 g g^{-1} at 80%, 65%, and 50% RH, respectively, in 12 h as illustrated in Fig. 3h. It also reached equilibrium within 12 h at 65% and 50% RH, demonstrating satisfactory kinetics. After 150 regeneration cycles, RTS shows no obvious loss in either water uptake capacity or kinetics (Supplementary Fig. 32), proving that the anti-crystallization ability provided by RTS can avoid pipeline blockage and thus ensure the stability of SLAB.

Design and optimization of water harvester

Based on the theoretical results, we designed a modular multi-stage water harvester for MSP2W, as depicted in Fig. 4a. The water harvester can be easily expanded to a multi-stage version modularly. Prototypes of the single-stage and dual-stage water harvester are illustrated in Fig. 4b. The triple-stage water harvester is shown in Supplementary Fig. 33. In this section, we employ electric heating as the heat source during desorption, as stable power input allows for precise characterization of MSAWH performance. We optimized the condenser flow channels using Multiphysics simulation, finding that a five-channel setup improved airflow uniformity and doubled water absorption compared to a single channel, with sorption kinetics experiments confirming the simulation results within a 10% error (Supplementary Fig. 34).

We first examine the harvester at 80% RH. As shown in Supplementary Fig. 36, over 1 day of operation, the single-stage harvester underwent three desorption and two absorption cycles, producing 1210 g of water. The moisture absorption showed negligible slowdown, indicating that the active SLAB and sufficient RTS maintained consistent absorption rates. In the first cycle, the SLAB absorbed 500 g of

https://doi.org/10.1038/s41467-025-66053-8

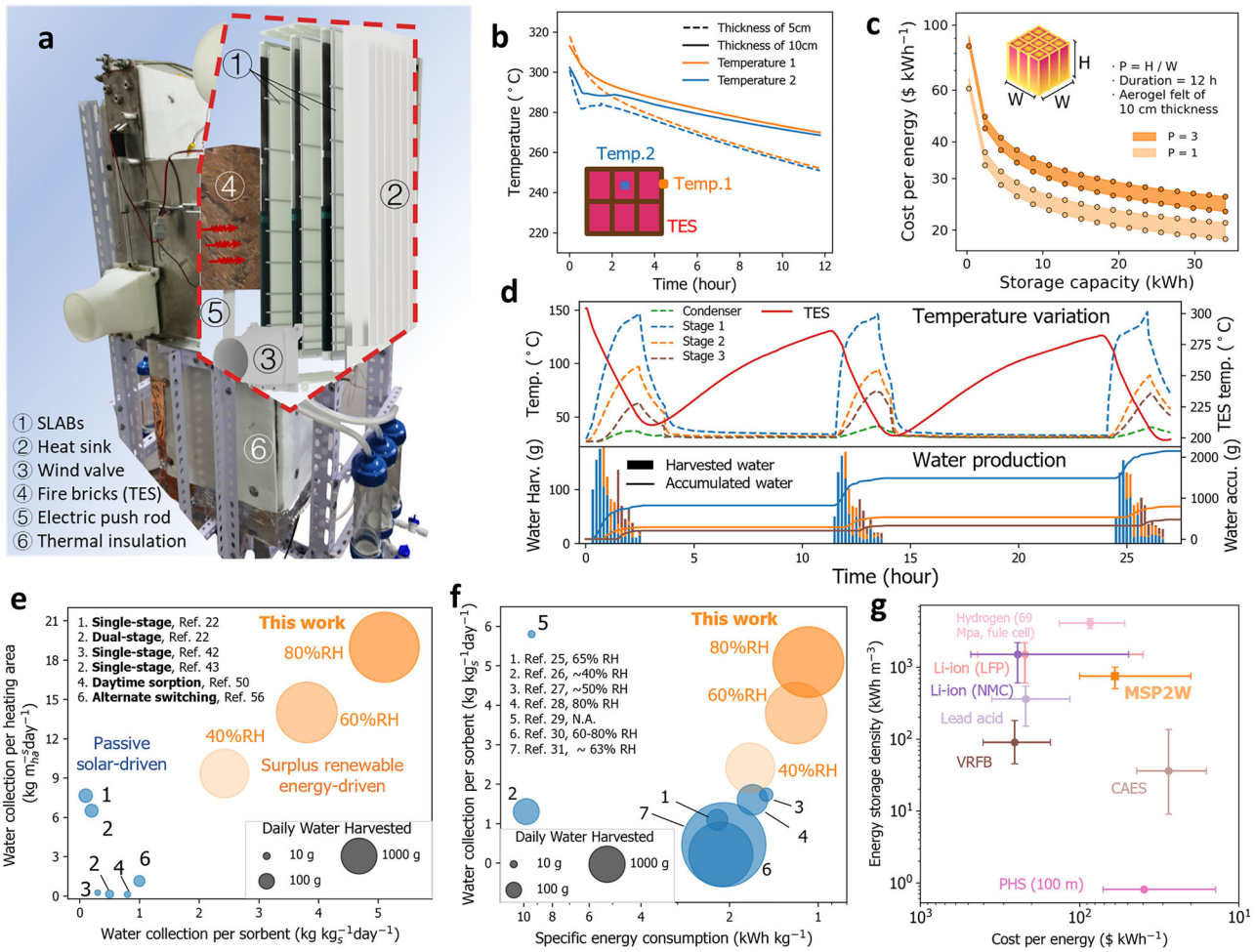

Fig. 5 | Performance of MSP2W battery. a Photo and cross-section schematic of a multi-stage water battery. Supplementary Fig. 46 for a complete photo without a cross-section. **b** Temperature variation of storage units in the energy storage process. The inset figure shows a top view of different measurement points. **c** The cost (measured in USD, $) of MgO-based TES variate with the storage capacity and height, and width proportion. The inset figure is schematic diagrams of the height and width proportion. The calculation methods can be referred to Supplementary Method 8. **d** Temperature variation and water production of triple-stage P2W battery. The upper figure shows the temperature of the sorbents and condenser; the lower figure shows the harvested and accumulated water. The experiment is shown in Supplementary Movie 4. **e** Comparison with state-of-the-art passive AWH technologies toward kinetics enhancement, in water collection per heating area and per sorbent, and daily water harvested. The details are given in Supplementary Table 6. **f** Comparison with state-of-the-art active AWH technologies in specific energy consumption, water collection per kg of sorbent, and daily water harvested. The details can be referred to in Supplementary Table 7. **g** Comparison of ESD and CPE for different ESSs[58,59]. Technologies plotted include hydrogen, Li-ion batteries (Lithium Iron Phosphate (LFP) and Nickel Manganese Cobalt (NMC)), lead acid batteries, vanadium redox flow batteries (VRFB), PHS, and CAES. The output electricity is considered to produce water by a vapor-compression heat pump with a COP of 3. Error bars represent the interquartile range, which defines the central 50% of probable values derived from the uncertainty in the input data.

moisture and produced 395 g of water during desorption, with a conversion rate of 80% and only ~20% vapor leakage due to clamping pressure. Adopting a three-cycle-per-day strategy increased water production by 15%, reaching 1388 g (Supplementary Fig. 37), while power consumption rose by 18%, from 2.01 to 2.37 kWh (Supplementary Fig. 37c). For the dual-stage system, total water production increased to 1661 g, with Stage 1 producing 1133 g and Stage 2 producing 528 g (Supplementary Fig. 42). The triple-stage system achieved 1829 g (Supplementary Fig. 45). Compared to the single-stage, the dual-stage system improved water production by 37.2% and reduced energy consumption by 21.1%. The triple-stage system improved water production by 51.2%, with the specific energy consumption decreased from 1.66 kWh kg^{-1} (single-stage) to 1.23 kWh kg^{-1} (triple-stage), showing a 26% improvement.

We further investigated the performance of the MSP2W system under arid environments. At 40% RH, the dual-stage and triple-stage systems achieved water production of 790 g and 810 g per day, outperforming the single-stage system (660 g day^{-1}) by 20% and 23%, respectively. Comprehensively considering the three humidity levels, the dual-stage and triple-stage yields are 31% and 40% higher than the single-stage, respectively (Fig. 4c). In terms of energy efficiency, as shown in Fig. 4d, at 60% RH, the specific energy consumption decreased from 1.85 kWh kg^{-1} (single-stage) to 1.42 kWh kg^{-1} (dual-stage) and 1.45 kWh kg^{-1} (triple-stage), showing about 21% improvement. At 40% RH, the specific energy consumption decreased from 2.43 kWh kg^{-1} (single-stage) to 2.21 kWh kg^{-1} (dual-stage), while the triple-stage system increased to 2.35 kWh kg^{-1}. These results demonstrate the multi-stage configuration's ability to optimize energy use. But in extremely arid regions, the dual-stage configuration outperforms configurations with more stages.

Performance of the MSP2W battery

The photo and cross-section schematic of the MSP2W battery prototype are depicted in Fig. 5a. The MSP2W battery incorporates two triple-stage water harvesters. The TES units consist of 25 kg magnesium oxide (MgO)-based fire bricks, with a storage capacity of 3.3 kWh

at a 300 °C temperature difference. Commercial high-purity MgO bricks, after extensive thermal tests, demonstrate excellent mechanical stability and chemical inertness, with negligible mechanical fatigue and chemical degradation in sub-400 °C TES applications[55,56]. An electric push rod, capable of vertical movement, drives the TES unit up and down. When lowered, the TES is enclosed within an insulation chamber wrapped with thermal insulation material (Supplementary Fig. 47). When the electric push rod extends, it propels the TES into the discharge chamber, allowing the stored thermal energy to be transferred to the harvester via radiation and conduction for desorption.

With 5 cm of thermal insulation covering the storage chamber, the TES loses 50 °C within 12 h. Increasing the insulation to 10 cm reduces this loss to 30 °C, which equates to about 10% of the stored energy, but the temperature of TES remains above 260 °C, ensuring efficient desorption (Fig. 5b). As shown in Fig. 5c, the TES demonstrates a remarkable scale effect. As the system scales up, the specific surface area and heat loss decrease, resulting in reduced self-discharge and improved stability and performance, with the energy storage cost reduced by 70% to 30 $ kWh^{-1}. Given its low-cost and non-degradable properties[16], the magnesium oxide-based TES is suitable for large-scale, short-term energy storage. As illustrated in Fig. 5d, during each desorption cycle, the TES temperature decreases by approximately 90 °C. At the same time, each desorption takes longer (about 2 h) compared with the MSAWH experiments in Supplementary Figs. 37–45. This shows that the MSP2W heating power is slightly smaller than the 350 W (heat flux of 2333 W m^{-2}) heating power in the previous section. We also calculate the potential energy loss based on the temperature distribution and provide an energy flow diagram, as shown in Supplementary Fig. 48, showing that over 90% of the stored energy is used for cascade AWH production.

The final daily water production totals 3060 g at 80% RH, averaging 1530 g per harvester, slightly lower than the triple-stage electric-heating water harvester discussed in Section 2.4. At 60% and 40% RH, the prototype produces 2320 and 1490 g water per day, respectively (Supplementary Fig. 50). We compare the water production per unit heating area and per unit mass of sorbent with the most advanced passive solar-driven AWH towards sorption kinetics enhancement, as shown in Fig. 5e[22,25,41,42,49,57]. Compared with the low production rates of passive AWH systems, MSP2W increases water production by utilizing excess renewable energy, making it more suitable for large-scale applications. MSP2W outperforms passive AWH systems even at arid conditions (40% RH), achieving production rates of 2.48 kg kg^{-1} sorbent and 4.9 kg m^{-2}. Furthermore, the prototype demonstrates scalability, with its production of 3060 g day^{-1} meeting the average daily requirement for an adult (2500 g day^{-1}), which all current passive AWH prototypes cannot do. Also, due to the multi-stage configuration and cascade usage of energy, the MSP2W has total power consumption of 3.46 kWh, 3.02 kWh, and 2.71 kWh (Supplementary Fig. 51) and specific power consumption of 1.13, 1.29, and 1.81 kWh kg^{-1} at 80%, 60%, and 40% RH, respectively, which is a record low for state-of-the-art active AWH technologies, as illustrated in Fig. 5f[25–31]. Moreover, the concentrations of dissolved ions in the collected water are measured (Supplementary Fig. 52), and the results confirm that the quality of the water meets the World Health Organization's standards for drinking water. Additionally, the SLAB enables MSP2W to exhibit rapid kinetics, fully utilizing the loaded sorbent and achieving a satisfactory water production rate of 5.1 kg day^{-1} per kg sorbent. We also calculate the gap between experimental and theoretical limits. Considering there are three desorptions, the water production limit at 80% RH is 19.2 kg m^{-2} day^{-1}. The experiment production is 10.2 kg m^{-2} day^{-1} (Supplementary Table 6). Therefore, the experiment-theory ratio is about 53%. The reason could be the limited time of absorption and desorption, so that the sorbent cannot reach equilibrium. Also, even if we consider the scenario of using an electrically driven vapor-compression heat pump with COP = 3 to condense water vapor in the air, MSP2W achieves higher energy storage density (ESD) while maintaining a lower cost per energy (CPE) than most traditional ESSs like Li-ion batteries, hydrogen storage, and even the terrain-reliable compressed air energy storage (CAES), and pumped hydro storage (PHS), suggesting that MSP2W potentially offers a more efficient and economical solution for energy storage, making it a compelling option in the energy sector (Fig. 5g).

Global AWH potential assessment and niche area

Water scarcity mitigation potential (WSMP) quantifies the ability of renewable energy to alleviate local water scarcity using MSP2W technology (Fig. 6a). It is calculated by comparing the regional renewable energy potential with the regional water demand, factoring in the efficiency of MSP2W (Supplementary Method 1). A higher WSMP value indicates greater potential for MSP2W to mitigate water scarcity. Based on Fig. 6a, the WSMP map clearly illustrates the potential application of MSP2W technology in various regions. The map shows that areas with WESI > 0.25 have significant potential for the MSP2W system, as these regions not only face considerable water scarcity but also possess abundant renewable energy resources. Specifically, regions (e.g., Central Asia and Southern Europe) with a WSMP > 1 indicate that MSP2W technology could theoretically use local renewable energy to completely solve the local water scarcity. Notably, northwest China, North Africa, the western United States, and the Middle East show a WSMP value greater than 100, suggesting that these regions could fully address their water shortage using less than 1% of local renewable energy and MSP2W technology. Other regions, such as South America, South Asia, and Southeast Asia, have WSMP values close to or slightly below 1, indicating that these areas also have considerable potential to improve water access through MSP2W, especially during dry seasons or peak water demand periods. Although WSMP values represent theoretical upper limits. Actual performance will be constrained by local factors such as the actual ambient conditions, the availability of energy infrastructure, resource variability, and others. But WSMP still should be interpreted as a useful orientation tool, highlighting the broad applicability of MSP2W technology in tackling the global water crisis.

A key factor influencing the economics of MSP2W is the timing of low-price renewable energy, such as the deep valley and clearance period observed in regions like Xinjiang. During these periods, MSP2W can operate at exceptionally low energy costs, sometimes even negative prices. As shown in Supplementary Table 9, during deep-low-price and clearance periods, the energy costs for MSP2W can be as low as 4.25 USD ton^{-1} and 0.44 USD ton^{-1}, respectively. Additionally, we calculate the levelized cost of water (LCW) of MSP2W under varying electricity price scenarios, using a dynamic model that explicitly accounts for time-varying electricity prices, location-specific tariffs, capital costs, and overall water-production efficiency. Figure 6b, c shows that relative humidity has modest LCW sensitivity. Because at higher RH, the sorbent begins to desorb before reaching near-equilibrium, and at low uptakes, kinetic differences are limited (Fig. 3h), so RH is secondary to price/utilization. Besides, as the charging power or the capacity of the energy storage unit increases, LCW falls steeply (fully utilizing low-priced renewable energy) to an optimum LCW (~10–20 USD ton^{-1}) and then rises when power/storage becomes misaligned with available power/energy windows and sorption capacity. Thus, sizing of charging power and storage capacity should be context-specific and optimized.

Geographically speaking, Fig. 6b, c shows that the LCW of MSP2W in Spain is slightly higher than that of Xinjiang. In contrast, as the charging power increases, the LCW of California becomes markedly lower than both (<10 USD ton^{-1}), even dipping below that of desalination technologies, such as reverse osmosis (RO) and multi-stage flash distillation. This behavior reflects the market structures

https://doi.org/10.1038/s41467-025-66053-8

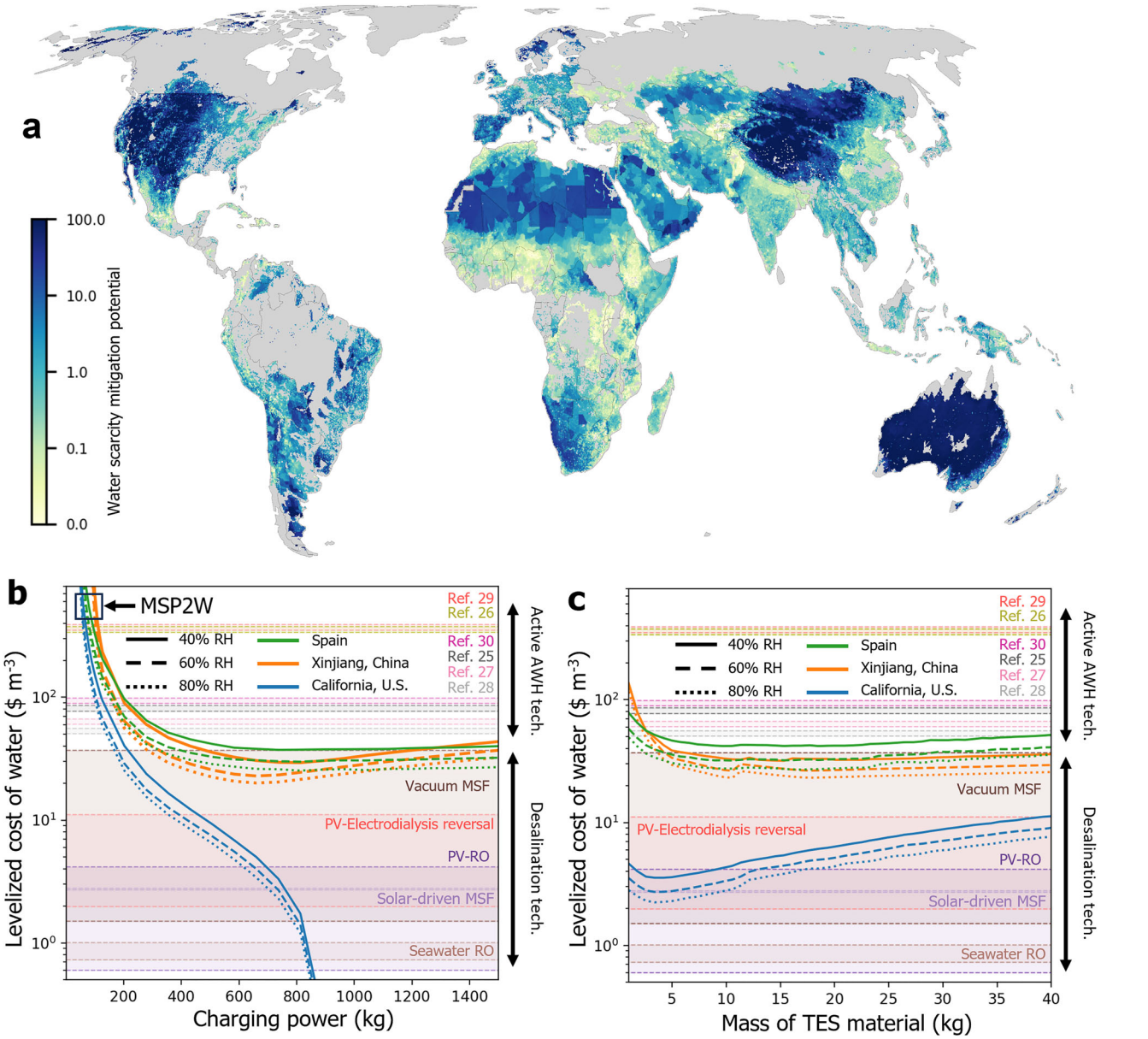

Fig. 6 | Global water scarcity mitigation potential (WSMP) assessment and levelized cost of water of MSP2W. a WSMP assessment of the MSP2W battery. The map highlights regions with WESI > 0.25, where MSP2W technology could significantly alleviate water scarcity by utilizing renewable energy sources. Areas with WSMP > 1 theoretically have the potential to fully resolve water shortages by providing 185 tons of water per person per year. The calculation details are presented in Supplementary Method 1. **b** The levelized cost of water with variable charging power of the MSP2W battery compared with the existing active AWH technologies and desalination technologies. **c** The levelized cost of water with variable thermal energy storage capacity of the MSP2W battery compared with the existing active AWH technologies and desalination technologies. The calculation details are presented in Supplementary Method 9.

quantified in Supplementary Table 9: California exhibits frequent negative-price hours (882 h year^{-1}), while Spain has fewer negative hours and a higher mean price. Because MSP2W follows a joule-heating route, increasing the charging power has a low marginal cost yet enhances the ability to capture short, low- or negative-price windows. Hence, LCW declines most strongly in California. The same pattern persists when varying TES mass (Fig. 6c). Besides, Supplementary Fig. 53 shows that LCW is weakly sensitive to the electric heater and TES prices but strongly to the sorbent cost and device lifespan. Thus, choosing an inexpensive, high uptake sorbent such as RTS is pivotal, and durability and maintainability are essential to sustain low LCW. Therefore, the model confirms that MSP2W outperforms existing active AWH systems and rivals desalination technologies, avoiding high capital costs, membrane fouling, and brine disposal issues. The niche ability of MSP2W to store energy and operate during off-peak hours significantly enhances its economic viability, allowing it to utilize even short, low-price windows fully. This capability decouples the system from the intermittency of renewable energy sources, ensuring consistent and cost-effective water production.

Discussion

MSP2W battery combines energy storage and AWH, particularly suitable for regions abundant in renewable energy yet scarce in freshwater resources. Unlike conventional ESSs that store and release electricity, MSP2W functions as a battery in a broader sense by storing surplus renewable energy in one form (thermal) and converting it into freshwater. This capability underlines the niche that MSP2W occupies, offering an effective solution to both grid stability and water scarcity. However, to realize its full practical potential, several critical issues still require attention.

One notable limitation is the performance of MSP2W under extremely low humidity conditions, specifically when the RH falls below 30%. As demonstrated by our experiments, water production significantly decreases at lower humidity due to the diminished sorption capacity, although the high heat flux brought by high-temperature TES can ensure a higher yield than passive AWH technology. To mitigate this issue, adopting a single-stage or dual-stage configuration could be more suitable. Additionally, integrating supplemental humidity sources, such as cooling tower exhaust, could help increase local humidity levels during dry periods.

The choice of sorbent material directly affects water sorption capacity, energy efficiency, and the system's ability to function under varying environmental conditions. As shown in our work, we explore RTS that could provide higher sorption capacities and improved sorption kinetics. However, there is still much room for improvement in the development of these sorbents in high cost-effectiveness and ultra-long-term durability. More crystallization-resistant and more stable RTS can be explored in the future.

Despite these challenges, MSP2W addresses two intertwined global challenges—renewable energy curtailment and freshwater scarcity. By converting otherwise wasted surplus renewable energy into freshwater, MSP2W offers an economically attractive solution, particularly advantageous in regions with frequent renewable energy overproduction. Utilizing surplus energy available at minimal or even negative cost periods significantly reduces the cost of freshwater production, rendering MSP2W competitive compared to conventional methods like desalination, especially for off-grid and remote applications.

Methods

Fabrication and characterization of Reline-based ternary solution

LiCl (≥99%), ChCl (≥98%), and urea (≥99–100%) were procured from Macklin. Reline, a DES composed of ChCl and urea (1:2 molar ratio), was first prepared. The mixture was heated to 90 °C and stirred until a clear, uniform liquid formed. Subsequently, a 55% LiCl solution was also heated to 90 °C and stirred until it completely dissolved. Reline was slowly added to the LiCl solution according to the target mass fraction and stirred until a homogeneous solution (RTS-X) was obtained.

The crystallization point is determined by using the turbidimetric method, the accuracy of which is confirmed by comparing theoretical and experimental data on the crystallization point of LiCl (Fig. 3b). A specific mass fraction of the solution was heated and stirred at 100 °C until fully dissolved. It was then cooled slowly using a water bath magnetic stirrer set to a rate of 10 °C per hour. The crystallization point was defined as the temperature at which turbidity changed markedly (Supplementary Fig. 54). Infrared spectra of Reline, RTS, and LiCl solutions were recorded using a FTIR spectrometer (Nicolet 6700, Thermo Fisher). Sorption isotherms for RTS and Reline were measured with a vapor sorption analyzer (IGA 002, HIDEN Analytical, UK). Because the analyzer cannot test liquids directly, samples were prepared by impregnating cotton tissue with the liquid. Samples were purged in N_2 at 100 °C for 24 h prior to testing. The mass of the cotton substrate was subtracted during data analysis.

Fabrication and characterization of SLAB

The SLAB container was made of titanium and PTFE, with an inner depth of 4.5 mm. From inside to outside, the layers comprised 0.2 mm cotton tissue, 4 mm carbon foam (Guangshengjia Metal New Materials), and 1 mm ACFF (Jingzhou Haote New Materials). The outer layer was a hydrophobic, breathable PTFE membrane (AORPF-RBH04HZ and AORPF-RBH1DT, 1 μm pore size; Cobetter). FTIR and contact angle data are shown in Supplementary Fig. 55. The membrane was sealed to the container with food-grade silicone, and 2 mm holes were drilled on the top to insert long PTFE tubes. During absorption, the solution was circulated and cooled via a titanium-finned tube using a peristaltic pump. The cooled solution entered the engraved top grooves for uniform distribution and mixing. A 304 stainless steel frame supported the outer PTFE membrane.

A scaled-down 22 × 11 cm SLAB was employed for sorption kinetics testing. Unless stated otherwise, airflow was supplied at a 45° angle. Air velocity near the SLAB surface was measured with a hot-wire anemometer (ST866A, SMART). A solution containing 20 g of sorbent was prepared before testing, unless specified otherwise. Before testing, the SLAB was placed overnight in a forced air-drying oven (202-0A, Shangcheng) set at 110 °C. During the sorption kinetics test, the external circulation loop was removed, and the SLAB was weighed using an electronic balance hourly (YHM100001, Ying Heng). Ambient temperature and humidity were controlled with an air conditioner and dehumidifier.

Stability examination of SLAB loaded with RTS was performed in an environmental chamber (Supplementary Fig. 19a) with controlled temperature and humidity (26 °C and 60% RH). RTS is sealed in a scale-down SLAB. Heating power was regulated using a DC power supply (IT6831A) set to operate in a 10-min heating/50-min cooling cycle at 20 W. A polyimide resistive heater (40 × 40 × 0.3 mm) was used for heating. A K-type thermocouple fixed at the center of the SLAB bottom measured temperature and was connected to a data acquisition system (34970A, Agilent). The heater was mounted on porous insulating foam (100 × 100 × 50 mm) to minimize heat loss from the back. Mass changes during desorption and absorption were continuously monitored using a high-precision electronic balance (ME503TTE, Mettler Toledo).

Fabrication and characterization of a multi-stage water harvester

A full-size SLAB (50 × 30 cm) was integrated into a multi-stage water harvester comprising air valves, a sealed frame, an air-channel condenser, a heat sink, and SLABs. A 3D-printed fiberglass air valve driven by an electric push rod enabled automatic switching between absorption and desorption, which can convert vertical force from the push rod into horizontal compression of a rubber pad to seal the unit, sealing the system during desorption (Supplementary Fig. 56). The external frame was made of heat-insulating PTFE, and gaps were sealed with food-grade silicone. Bolts applied preload to compress the silicone for tight sealing. Aluminum outer fins with a 20 W fan enhanced forced convective cooling. Each stage used a 10 W centrifugal fan to increase inlet airflow. Thermocouples were placed 5 cm behind each SLAB stage, and outlet temperature and humidity were monitored. A smart socket recorded the power consumption of pumps, fans, and heaters, excluding data acquisition and control systems. The five-air-channel condenser distributed airflow evenly to avoid short-circuiting (Supplementary Fig. 34c).

Outlet wind speed was measured using a hot-wire anemometer. Based on this, the air volume V_a ($m^3\ s^{-1}$) is calculated using the following formula:

$$V_a = HWv \tag{2}$$

where H is the height of the outlet of the wind valve, 5.2 cm; W is the width of the outlet of the wind valve, 2.7 cm; v is the velocity of outlet airflow, $m\ s^{-1}$. The harvested moisture is calculated using this formula:

$$M_h = \rho V_a(h_{in} - h_{out}) \tag{3}$$

where M_h is the mass of harvested water, $g\ s^{-1}$; h_{in} and h_{out} represent the humidity of the inlet and outlet, respectively, $gkg^{-1}_{dry\ air}$; ρ is the density of air, $kg\ m^{-3}$.

Sorbent loading was 150 g, 100 g, and 50 g for stages 1, 2, and 3, respectively. Unless stated otherwise, two absorption–desorption cycles per day were performed, with ~10 h absorption time. A 300 W electric heater facilitated desorption and was stopped when stage 1 reached 145 °C, the Reline decomposition temperature (Supplementary Fig. 57). Water production was recorded every 10 min using a scaled tank. Ambient temperature and RH were maintained at ~27 °C.

Fabrication and characterization of MSP2W battery

Magnesium oxide fire bricks weighing 25 kg were utilized as the TES medium (Supplementary Fig. 58). Six 50 W heating rods with thermocouples were inserted into drilled holes on the top of the brick, with gaps sealed using high-temperature inorganic glue and fixed by screws. A 5 mm copper plate was attached to the brick surface facing the harvester to improve heat uniformity and sealing (Supplementary Fig. 59). The plate was coated with a high-emissivity graphene layer (Graphene Star, Nakait New Materials) to improve radiative heat transfer to the harvester. The copper plate can also fill in the gap between the water harvester and the TES unit. The distance between the copper plate and the harvester is less than 1 mm. The TES chamber was insulated with 5–10 cm aerogel fiberboard lined with reflective aluminum sheets (Supplementary Fig. 60).

During charging, an 18 W axial fan ventilated all harvester stages. The TES was heated with 150 W, without fully activating all rods, allowing the TES to gradually reach ~300 °C while using inactive rods as temperature probes. To protect the rods, the TES temperature limit was set to 300 °C, as higher values could raise internal temperatures above 600 °C.

During the discharge stage, the MSP2W system closed the air valve, and the TES unit was propelled into the desorption chamber by an electric push rod. In this position, the TES maintained close contact with the water harvester, facilitating heat transfer to the harvester primarily through conduction and radiation. Water released during this process was collected in a scaled water storage tank, with water production recorded at 10-min intervals. An Ion Chromatography system (ICS–1100, Dionex) was used to detect concentrations of possible metals and ions in the collected water.

Data availability

The data supporting the findings of the study are included in the main text and the Supplementary Information file. The experimental data generated in this study are available as provided in the Source data file. Other raw data can be obtained from the corresponding author upon request. Source data are provided with this paper.

Code availability

The code supporting this study, including a dynamic simulation model, the climate-based quantification + IEA data correction workflow, and cost modeling, is publicly available in an executable Code Ocean capsule (https://doi.org/10.24433/CO.4056554.v2).

References

1. Chu, S. & Majumdar, A. Opportunities and challenges for a sustainable energy future. *Nature* **488**, 294–303 (2012).
2. Ziegler, M. S. et al. Storage requirements and costs of shaping renewable energy toward grid decarbonization. *Joule* **3**, 2134–2153 (2019).
3. Gür, T. M. Review of electrical energy storage technologies, materials and systems: challenges and prospects for large-scale grid storage. *Energy Environ. Sci.* **11**, 2696–2767 (2018).
4. Sternberg, A. & Bardow, A. Power-to-What? – Environmental assessment of energy storage systems. *Energy Environ. Sci.* **8**, 389–400 (2015).
5. Kavadias, K. & Triantafyllou, P. Wind-Based Stand-Alone Hybrid Energy Systems. In *Comprehensive Renewable Energy* 2nd edn (ed. Letcher, T. M.) 749–793 (Elsevier, 2022).
6. Beuse, M., Steffen, B. & Schmidt, T. S. Projecting the competition between energy-storage technologies in the electricity sector. *Joule* **4**, 2162–2184 (2020).
7. Greim, P., Solomon, A. A. & Breyer, C. Assessment of lithium criticality in the global energy transition and addressing policy gaps in transportation. *Nat. Commun.* **11**, 4570 (2020).
8. Gur, I., Sawyer, K. & Prasher, R. Searching for a better thermal battery. *Science* **335**, 1454–1455 (2012).
9. Benato, A. & Stoppato, A. Pumped thermal electricity storage: a technology overview. *Therm. Sci. Eng. Prog.* **6**, 301–315 (2018).
10. Braff, W. A., Mueller, J. M. & Trancik, J. E. Value of storage technologies for wind and solar energy. *Nat. Clim. Change* **6**, 964–969 (2016).
11. Caldera, U. & Breyer, C. Afforesting arid land with renewable electricity and desalination to mitigate climate change. *Nat. Sustain.* **6**, 526–538 (2023).
12. Poredoš, P., Shan, H., Wang, C., Deng, F. & Wang, R. Sustainable water generation: grand challenges in continuous atmospheric water harvesting. *Energy Environ. Sci.* **15**, 3223–3235 (2022).
13. Lord, J. et al. Global potential for harvesting drinking water from air using solar energy. *Nature* **598**, 611–617 (2021).
14. Song, Y. et al. Hierarchical engineering of sorption-based atmospheric water harvesters. *Adv. Mater.* **36**, 2209134 (2024).
15. Entezari, A., Esan, O. C., Yan, X., Wang, R. & An, L. Sorption-based atmospheric water harvesting: materials, components, systems, and applications. *Adv. Mater.* **35**, 2210957 (2023).
16. Lin, H. et al. Versatile power-to-water battery for energy storage, atmospheric water harvesting, and humidity control. *ACS Appl. Mater. Interfaces* **15**, 36107–36116 (2023).
17. Wang, X. et al. An interfacial solar heating assisted liquid sorbent atmospheric water generator. *Angew. Chem. Int. Ed.* **58**, 12054–12058 (2019).
18. Qi, H. et al. An interfacial solar-driven atmospheric water generator based on a liquid sorbent with simultaneous adsorption–desorption. *Adv. Mater.* **31**, 1903378 (2019).
19. Hanikel, N., Prévot, M. S. & Yaghi, O. M. MOF water harvesters. *Nat. Nanotechnol.* **15**, 348–355 (2020).
20. Song, Y. et al. High-yield solar-driven atmospheric water harvesting of metal–organic-framework-derived nanoporous carbon with fast-diffusion water channels. *Nat. Nanotechnol.* **17**, 857–863 (2022).
21. Krajnc, A. et al. Superior performance of microporous aluminophosphate with LTA topology in solar-energy storage and heat reallocation. *Adv. Energy Mater.* **7**, 1601815 (2017).
22. LaPotin, A. et al. Dual-stage atmospheric water harvesting device for scalable solar-driven water production. *Joule* **5**, 166–182 (2021).
23. Lu, H. et al. Tailoring the desorption behavior of hygroscopic gels for atmospheric water harvesting in arid climates. *Adv. Mater.* **34**, 2205344 (2022).
24. Matsumoto, K., Sakikawa, N. & Miyata, T. Thermo-responsive gels that absorb moisture and ooze water. *Nat. Commun.* **9**, 2315 (2018).
25. Shan, H. et al. Exceptional water production yield enabled by batch-processed portable water harvester in semi-arid climate. *Nat. Commun.* **13**, 5406 (2022).
26. Hanikel, N. et al. Rapid cycling and exceptional yield in a metal-organic framework water harvester. *ACS Cent. Sci.* **5**, 1699–1706 (2019).
27. Almassad, H., Abaza, R., Siwwan, L., Al-Maythalony, B. & Cordova, K. Environmentally adaptive MOF-based device enables continuous self-optimizing atmospheric water harvesting. *Nat. Commun.* **13**, 4873 (2022).

28. Min, X. et al. High-yield atmospheric water harvesting device with integrated heating/cooling enabled by thermally tailored hydrogel sorbent. *ACS Energy Lett.* **8**, 3147–3153 (2023).
29. Li, X. et al. Design of a compact multicyclic high-performance atmospheric water harvester for arid environments. *ACS Energy Lett.* 3391–3399. https://doi.org/10.1021/acsenergylett.4c01061 (2024).
30. Wang, W. et al. Air-cooled adsorption-based device for harvesting water from island air. *Renew. Sustain. Energy Rev.* **141**, 110802 (2021).
31. Wang, W. et al. All-day freshwater production enabled by an active continuous sorption-based atmospheric water harvesting system. *Energy Convers. Manag.* **264**, 115745 (2022).
32. Xu, Z. et al. Ultrahigh-efficiency desalination via a thermally-localized multistage solar still. *Energy Environ. Sci.* **13**, 830–839 (2020).
33. Zhang, L. et al. Modeling and performance analysis of high-efficiency thermally-localized multistage solar stills. *Appl. Energy* **266**, 114864 (2020).
34. Zhang, Z. et al. Thermal batteries based on inverse barocaloric effects. *Sci. Adv.* **9**, eadd0374. https://doi.org/10.1126/sciadv.add0374.
35. Department of Energy's Oak Ridge National Laboratory. Carbon batteries store renewable energy and help protect the climate. https://www.ornl.gov/news/carbon-capture-batteries-developed-store-renewable-energy-help-climate (2024).
36. Smith, E. L., Abbott, A. P. & Ryder, K. S. Deep eutectic solvents (DESs) and their applications. *Chem. Rev.* **114**, 11060–11082 (2014).
37. Kołaski, M. et al. Structures, energetics, and spectra of aqua-cesium (I) complexes: An ab initio and experimental study. *J. Chem. Phys.* **126**, 074302 (2007).
38. Mishra, R. et al. Role of Intermolecular Interactions in deep eutectic solvents for CO2 capture: vibrational spectroscopy and quantum chemical studies. *J. Phys. Chem. B* **128**, 10214–10229 (2024).
39. Araújo, C. F. et al. Good vibrations: understanding deep eutectic solvents through the lens of vibrational spectroscopy. *Appl. Spectrosc. Rev.* **60**, 137–192 (2025).
40. Honda, A., Nozawa, R. & Miyamura, K. Molecular aggregation by hydrogen bonding in cold-crystallization behavior of mixed nucleobases analyzed by temperature-controlled infrared spectroscopy. *RSC Adv.* **14**, 3776–3781 (2024).
41. Kim, H. et al. Water harvesting from air with metal-organic frameworks powered by natural sunlight. *Science* **356**, 430–434 (2017).
42. Xu, J. et al. Efficient solar-driven water harvesting from arid air with metal–organic frameworks modified by hygroscopic salt. *Angew. Chem. Int. Ed.* **59**, 5202–5210 (2020).
43. Rieth, A. J., Yang, S., Wang, E. N. & Dincă, M. Record atmospheric fresh water capture and heat transfer with a material operating at the water uptake reversibility limit. *ACS Cent. Sci.* **3**, 668–672 (2017).
44. Yang, J. et al. A moisture-hungry copper complex harvesting air moisture for potable water and autonomous urban agriculture. *Adv. Mater.* **32**, 2002936 (2020).
45. Nandakumar, D. K. et al. Solar energy triggered clean water harvesting from humid air existing above sea surface enabled by a hydrogel with ultrahigh hygroscopicity. *Adv. Mater.* **31**, 1806730 (2019).
46. Towsif Abtab, S. M. et al. Reticular chemistry in action: a hydrolytically stable MOF capturing twice its weight in adsorbed water. *Chem* **4**, 94–105 (2018).
47. Nguyen, H. L. et al. A porous covalent organic framework with voided square grid topology for atmospheric water harvesting. *J. Am. Chem. Soc.* **142**, 2218–2221 (2020).
48. Yang, K., Pan, T., Pinnau, I., Shi, Z. & Han, Y. Simultaneous generation of atmospheric water and electricity using a hygroscopic aerogel with fast sorption kinetics. *Nano Energy* **78**, 105326 (2020).
49. Li, R., Shi, Y., Wu, M., Hong, S. & Wang, P. Improving atmospheric water production yield: enabling multiple water harvesting cycles with nano sorbent. *Nano Energy* **67**, 104255 (2020).
50. Zhao, F. et al. Super moisture-absorbent gels for all-weather atmospheric water harvesting. *Adv. Mater.* **31**, 1806446 (2019).
51. Karmakar, A. et al. Thermo-responsive MOF/polymer composites for temperature-mediated water capture and release. *Angew. Chem. Int. Ed.* **59**, 11003–11009 (2020).
52. Yang, K. et al. Hollow spherical SiO_2 micro-container encapsulation of LiCl for high-performance simultaneous heat reallocation and seawater desalination. *J. Mater. Chem. A* **8**, 1887–1895 (2020).
53. Kallenberger, P. A. & Fröba, M. Water harvesting from air with a hygroscopic salt in a hydrogel-derived matrix. *Commun. Chem.* **1**, 28 (2018).
54. Yao, H. et al. Highly efficient clean water production from contaminated air with a wide humidity range. *Adv. Mater.* **32**, 1905875 (2020).
55. Yang, M. et al. Enhanced performance of ultra-low carbon MgO–C bricks by the addition of special C/$MgAl_2O_4$ composite powders. *Ceram. Int.* **48**, 24411–24420 (2022).
56. Lagorio, Y. S., Gass, S. E., Benavidez, E. R. & Tomba Martínez, A. G. Thermomechanical evaluation of MgO–C commercial bricks. *Ceram. Int.* **48**, 10105–10112 (2022).
57. Xu, J. et al. Ultrahigh solar-driven atmospheric water production enabled by scalable rapid-cycling water harvester with vertically aligned nanocomposite sorbent. *Energy Environ. Sci.* **14**, 5979–5994 (2021).
58. Zakeri, B. & Syri, S. Electrical energy storage systems: A comparative life cycle cost analysis. *Renew. Sustain. Energy Rev.* **42**, 569–596 (2015).
59. Mongird, K. et al. 2020 grid energy storage technology cost and performance assessment. 25 (Pacific Northwest National Laboratory, 2020).

Acknowledgements

This work is jointly supported by the National Natural Science Foundation of China (Nos. 52322812 to W.W., 52476019 to W.W., 52573247 to Y. Song, 52525202 to J.Z., 52461160296 to J.Z.), the Shenzhen Science and Technology Program (No. JCYJ20230807114905012 to W.W.), the Research Grants Council of Hong Kong (No. CityU 11218922 to W.W.), the Environment and Conservation Fund of Hong Kong (No. 76/2022 to W.W.), National Key R&D Program of China (No. 2024YFF0506000 to J.Z.), and GeoX' Interdisciplinary Project of Frontiers Science Center for Critical Earth Material Cycling (No. 20250107 to Y. Song). J.Z. has been supported by the Meituan Green Tech Fund. The authors acknowledge the microfabrication center at the National Laboratory of Solid State Microstructures (NLSSM) for technical support. Any opinions, findings, conclusions, or recommendations expressed in this material/event do not necessarily reflect the views of the Government of the Hong Kong Special Administrative Region and the Environment and Conservation Fund.

Author contributions

H.L. and W.W. originated the concept. All authors contributed improvements to the presented idea. H.L. designed the experiment. H.L. made the simulations. H.L. and Y Sui prepared the used materials; Y. Song, Y Sui, Z.S., Z.D., and F.L. aided in interpreting the results. H.L., Z.D., and Y Song. wrote the manuscript with support from W.W. and J.Z. W.W., and J.Z. proposed revisions to the manuscript and supervised the findings of this work. All authors discussed the results and commented on the manuscript.

Competing interests

W.W. and H.L. are inventors of a US non-provisional patent application (No. US 20/2024/0286075 A1) filed on 31 July 2023 by City University of Hong Kong. The application covers the sorption–desorption control and TES-coupling system described in this manuscript. Apart from this patent application, the authors declare no other financial or non-financial competing interests.

Additional information

Supplementary information The online version contains supplementary material available at https://doi.org/10.1038/s41467-025-66053-8.

Correspondence and requests for materials should be addressed to Jia Zhu or Wei Wu.

Peer review information *Nature Communications* thanks Wei He, Zuankai Wang, and the other, anonymous, reviewer(s) for their contribution to the peer review of this work. A peer review file is available.